VUV-UV-vis photoluminescence, X-ray radioluminescence and energy transfer dynamics of Ce^{3+} and Eu^{2+} in $Sr_2MgSi_2O_7$

Wen, Donghao; Li, Quanfeng; Ou, Yiyi; Yang, Yunlin; Qi, Zeming; Dorenbos, Pieter; Liang, Hongbin

DOI
10.1039/d2dt03165e

Publication date
2022

Document Version
Final published version

Published in
Dalton Transactions

Dalton Transactions

ROYAL SOCIETY OF CHEMISTRY

PAPER

View Article Online
View Journal | View Issue

Cite this: *Dalton Trans.*, 2022, **51**, 17809

VUV-UV-vis photoluminescence, X-ray radioluminescence and energy transfer dynamics of Ce^{3+} and Eu^{2+} in $Sr_2MgSi_2O_7$†

Donghao Wen,[a] Quanfeng Li,[a] Yiyi Ou,[a] Yunlin Yang,[a] Zeming Qi,[b] Pieter Dorenbos[c] and Hongbin Liang *[a]

Received 29th September 2022,
Accepted 28th October 2022

DOI: 10.1039/d2dt03165e

rsc.li/dalton

Ce^{3+} and Eu^{2+} doped and Ce^{3+}–Eu^{2+} co-doped $Sr_2MgSi_2O_7$ phosphors are prepared *via* a high-temperature solid-state reaction technique. The synchrotron radiation vacuum ultraviolet-ultraviolet (VUV-UV) excitation and ultraviolet-visible (UV-vis) emission spectra of diluted Ce^{3+} and Eu^{2+} doped $Sr_2MgSi_2O_7$ samples are measured at cryogenic temperatures. The electron-vibrational interaction (EVI) between Ce^{3+} and its surroundings is analyzed. The dependencies of the 4f–5d transitions of Ce^{3+} on the structure of the host compounds $Sr_2MgSi_2O_7$, $Ba_2MgSi_2O_7$ and $BaMg_2Si_2O_7$ are discussed in detail. Then the thermal quenching channel is proposed based on the measurements of temperature dependent luminescence intensities and decay times of Ce^{3+} and Eu^{2+} in $Sr_2MgSi_2O_7$, and the $Ce^{3+} \rightarrow Eu^{2+}$ energy transfer mechanism is understood by three luminescence dynamic models. In addition, $Sr_2MgSi_2O_7$:Ce^{3+}/Eu^{2+} samples are evaluated for the possibilities of X-ray detection applications using X-ray excited luminescence (XEL) spectroscopy, and it was found that they are not suitable.

1. Introduction

Luminescence of Ce^{3+} and Eu^{2+} plays an important role in the detection of ionizing radiation due to their parity-allowed 4f–5d transitions. Numerous inorganic compounds doped with Ce^{3+} or Eu^{2+} ions have been widely studied, and materials such as Lu_2SiO_5:Ce^{3+} and SrI_2:Eu^{2+} with outstanding luminescence properties are commercially available scintillators.[1] In addition, materials like $Y_3Al_5O_{12}$:Ce^{3+} and $BaMgAl_{10}O_{17}$:Eu^{2+} serve successfully as yellow and blue emitting phosphors in light-emitting diodes (LEDs) and tricolor tubes for lighting and displays, respectively.[2] To find novel luminescent materials and to improve their luminescence performances, much attention has been directed toward energy transfer (ET) from and to Ce^{3+} and Eu^{2+} ions.[3,4]

The composition and structure of a host compound are essential for the luminescence property of a phosphor, because it directly rules the 4f–5d transitions of Ce^{3+} and/or Eu^{2+} in this compound. Silicates are suitable as host compounds for the luminescence of lanthanide and transition metal ions.[5,6] $Sr_2MgSi_2O_7$ with akermanite structure is of particular interest to us in these silicates.[7–10] A similar composition of $Sr_2MgSi_2O_7$ to those of $Ba_2MgSi_2O_7$ and $BaMg_2Si_2O_7$, and the single Sr^{2+}/Ba^{2+} site in these compounds make $Sr_2MgSi_2O_7$ an appropriate choice for studying the composition and structure dependent 4f–5d transitions and energy transfer of Ce^{3+} and Eu^{2+} ions.

In this paper, synchrotron radiation VUV-UV excitation and UV-vis emission spectra are recorded to fully understand the 5d energies of Ce^{3+} in $Sr_2MgSi_2O_7$, and the electron–phonon coupling of Ce^{3+} is analyzed in consideration of its significant influences on luminescence performances such as the Stokes shift and the bandwidth. In particular, the impacts of coordination surroundings on the 5d energies and luminescence properties of Ce^{3+} ions are systematically discussed for three compounds $Sr_2MgSi_2O_7$, $Ba_2MgSi_2O_7$ and $BaMg_2Si_2O_7$ with similar compositions. Furthermore, the thermal quenching channel of Ce^{3+} and Eu^{2+} ions, and the Ce^{3+}–Eu^{2+} energy transfer dynamics in $Sr_2MgSi_2O_7$ are discussed in detail. Finally, XEL measurements are performed to assess the application possibilities of Ce^{3+} and Eu^{2+} doped phosphors for X-ray detection.

2. Experimental

2.1 Sample preparation

Three series of powder samples, $Sr_{2-2x}Ce_xNa_xMgSi_2O_7$ (x = 0, 0.001, 0.005, 0.03), $Sr_{2-x}Eu_xMgSi_2O_7$ (x = 0.001, 0.003) and

[a]*MOE Key Laboratory of Bioinorganic and Synthetic Chemistry, KLGHEI of Environment and Energy Chemistry, School of Chemistry, Sun Yat-sen University, Guangzhou 510006, China*
[b]*National Synchrotron Radiation Laboratory, University of Science and Technology of China, Hefei 230029, China*
[c]*Faculty of Applied Sciences, Delft University of Technology, 2629 JB Delft, The Netherlands*

† Electronic supplementary information (ESI) available. See DOI: https://doi.org/10.1039/d2dt03165e

$Sr_{1.99-x}Ce_{0.005}Eu_xNa_{0.005}MgSi_2O_7$ (x = 0.001, 0.005, 0.01), were prepared *via* a high-temperature solid-state reaction technique. $SrCO_3$ (Analytical Reagent, A.R.), $4MgCO_3{\cdot}Mg(OH)_2{\cdot}5H_2O$ (A.R.), SiO_2 (99.99%), CeO_2 (99.99%), and Eu_2O_3 (99.99%) were used as the initial materials. 4 mol% H_3BO_3 (A.R.) was added as a flux, and the aliovalent substitution between trivalent Ce^{3+} and divalent Sr^{2+} in samples $Sr_{2-2x}Ce_xNa_xMgSi_2O_7$ and $Sr_{1.99-x}Ce_{0.005}Eu_xNa_{0.005}MgSi_2O_7$ was balanced by using monovalent Na^+ provided by Na_2CO_3 (99.99%) as charge compensators. The stoichiometric raw materials were ground in an agate mortar and then calcined at 1523 K for 4 h in a CO reducing ambience. The target products were obtained by grinding after cooling down to room temperature (RT).

2.2 Measurements

The phase purity of the samples was checked *via* the powder X-ray diffraction (XRD) technique using a Rigaku D-MAX 2200 VPC X-ray diffractometer with Cu Kα radiation (λ = 1.5418 Å) at 40 kV and 26 mA. The Rietveld structural refinement of the host compound was performed using the TOPAS-Academic program,[11] and then its high quality XRD data were collected using a Bruker D8 advanced X-ray diffractometer with Cu Kα radiation (λ = 1.5418 Å) at 40 kV and 40 mA with a step interval of 0.02°. The far infrared reflectance spectrum of the host compound was recorded on the BL01B beamline of the National Synchrotron Radiation Laboratory (NSRL, Hefei, China) at RT.[12]

An Edinburgh FLS1000 combined fluorescence lifetime and steady state spectrometer was used to record UV-vis excitation/emission spectra and luminescence decay curves. A 450 W xenon lamp was used as the excitation source for recording steady state luminescence spectra, and the excitation source used for obtaining luminescence decay curves was a 150 W nF900 lamp with a pulse width of 1 ns and a pulse rate of 40 kHz, or a 340 nm EPLED (picosecond pulsed light emitting diode) with a typical pulse width of 790 ps and a typical average power of 2.0 μW at 10 MHz, respectively. The temperature of the samples is controlled using a MercuryiTC Model temperature controller.

Synchrotron radiation VUV-UV excitation and corresponding emission spectroscopy were performed on the beamline 4B8 of the Beijing Synchrotron Radiation Facility (BSRF). XEL spectra were recorded using a Philips PW2253/20 X-ray tube at the Delft University of Technology, the Netherlands. More details can be found in ref. 13.

3. Results and discussion

3.1. XRD and crystal structure

The Rietveld refinement of the high-quality XRD data of the un-doped host compound $Sr_2MgSi_2O_7$ is first performed (Fig. S1(a)†). The acquired refinement parameters of R_p, R_{wp}, and R_{bragg} are 3.906%, 5.220%, and 2.710%, respectively, which prove the reliability of the result and purity of the sample. $Sr_2MgSi_2O_7$ has a tetragonal structure with the space group $P\bar{4}21m$. The lattice parameters are $a = b$ = 8.011 Å, c = 5.165 Å, and V = 331.4 Å^3. There is only one eight-fold coordinated Sr^{2+} site with C_1 symmetry in $Sr_2MgSi_2O_7$ and the average Sr^{2+}–O^{2-} bond length is 2.669 Å (Fig. S1(b)†).[7] The distance between the two nearest neighboring Sr^{2+} ions is 3.743 Å. The Mg^{2+} and Si^{4+} ions connect to four oxygen ions to form regular tetrahedra. Fig. S1(c)† depicts the crystal structure of $Sr_2MgSi_2O_7$, which is a layer structure arrangement in the c-axis direction. The Sr^{2+} ions form a layer separately, while the Mg^{2+} and Si^{4+} tetrahedra form another layer together between Sr^{2+} ions. Two $[SiO_4]^{2-}$ tetrahedra connect with each other *via* a corner-sharing oxygen ion and form a $[Si_2O_7]^{6-}$ cluster.

The XRD patterns of typical $Sr_2MgSi_2O_7$, $Sr_{2-2x}Ce_xNa_xMgSi_2O_7$ (x = 0.001, 0.03), $Sr_{2-x}Eu_xMgSi_2O_7$ (x = 0.001) and $Sr_{1.99-x}Ce_{0.005}Eu_xNa_{0.005}MgSi_2O_7$ (x = 0.01) samples at RT shown in Fig. S1(d)† match well with the standard card (PDF# 75-1736) of $Sr_2MgSi_2O_7$,[7] showing that the impurity phase content would be below the detection limit of XRD if it existed in the samples and demonstrating that Ce^{3+}, Eu^{2+} and Na^+ ions do not significantly change the crystal structure. Due to the similar ion radii of eight-fold coordinated Ce^{3+} (~1.14 Å), Na^+ (~1.18 Å), Eu^{2+} (~1.25 Å) and Sr^{2+} (~1.26 Å), the doped Ce^{3+}, Eu^{2+} and Na^+ ions are thought to occupy the Sr^{2+} sites in the samples.

3.2. Photoluminescence of Ce^{3+} in $Sr_2MgSi_2O_7$

Fig. S2† shows the height-normalized excitation spectra at different emission wavelengths (λ_{em} = 350, 368, 373 and 382 nm) and the height-normalized emission spectra at varying excitation wavelengths (λ_{ex} = 267, 272, 277, 319, 326 and 332 nm) of the sample $Sr_{1.998}Ce_{0.001}Na_{0.001}MgSi_2O_7$ at RT for comparison. It can be seen that either four normalized excitation curves or six normalized emission spectra well overlap each other, respectively. These phenomena indicate that the material does not contain impurities that affect the luminescence spectrum in this wavelength range, the doped Ce^{3+} ions occupy only one type of lattice site in the host compound and the inhomogeneous broadening of Ce^{3+} 4f–5d transitions does not occur in this diluted sample.[14] As mentioned above, we deem that Ce^{3+} ions are incorporated into eight-fold coordinated Sr^{2+} sites. The excitation peaks at approximately 326 and 273 nm result from the first and the second 4f–5d excitation bands of Ce^{3+} in this $[SrO_8]$ site of the host compound and their positions are in good agreement with those in Fig. 1 and close to those in references.[9,15] Two partially overlapped broad bands are seen in the emission curves and their peaks are at about 345 and 371 nm with an energy difference of about 0.24 eV (19.5×10^3 cm^{-1}). Obviously, these two bands correspond to the transitions from the relaxed lowest (the first) 5d to ^2F_J (J = 5/2, 7/2) states of Ce^{3+} ions in the Sr^{2+} sites of the host compound.

Fig. 1 displays the VUV-UV excitation (λ_{em} = 370 nm) and corresponding emission (λ_{ex} = 270 nm) spectra of the sample $Sr_{1.998}Ce_{0.001}Na_{0.001}MgSi_2O_7$ recorded by BSRF at 10 K. The typical broad doublet emission bands are at their maxima of about 345 and 368 nm in the emission spectrum, respectively. Their separation is clearer than that in Fig. S2† due to the

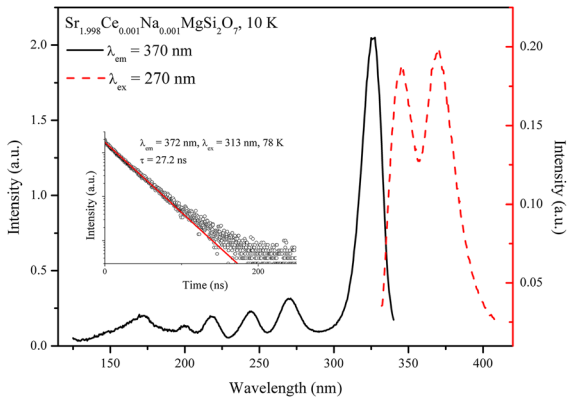

Fig. 1 The synchrotron radiation VUV-UV excitation (λ_{em} = 370 nm) and emission (λ_{ex} = 270 nm) spectra of the sample $Sr_{1.998}Ce_{0.001}Na_{0.001}MgSi_2O_7$ at 10 K. The inset shows its luminescence decay curve (λ_{ex} = 313 nm, λ_{em} = 372 nm) at 78 K.

measurement at a cryogenic temperature of 10 K in Fig. 1, and their peaks are consistent with those (about 345 and 371 nm) in Fig. S2.† As shown in the inset, the luminescence decay curve was exponential, and the decay time was estimated to be ~27.2 ns.

There are six distinct excitation bands in the VUV-UV excitation spectrum (the black solid line) in the range of 125–340 nm, which originate from the host-related absorption and the 4f–5d transitions of Ce^{3+}. The host related absorption band peaked at ~170 nm (7.29 eV, 58.8 × 10^3 cm^{-1}) is identified as the host exciton creation absorption energy E^{ex}. The band gap between the bottom of the conduction band and the top of the valence band is equal to this exciton creation energy plus the exciton binding energy. The empirical formula 0.008 × $(E^{ex})^2$ = 0.43 eV was used to estimate the exciton binding energy.[16] Then, the band gap of $Sr_2MgSi_2O_7$ was evaluated to be ~7.72 eV.

Four clear excitation bands at about 326 nm (3.80 eV, 30.7 × 10^3 cm^{-1}), 269 nm (4.61 eV, 37.2 × 10^3 cm^{-1}), 244 nm (5.08 eV, 41.0 × 10^3 cm^{-1}), and 217 nm (5.71 eV, 46.1 × 10^3 cm^{-1}) and a relatively weak band at about 200 nm (6.20 eV, 50.0 × 10^3 cm^{-1}) were observed in the 190–340 nm range of the excitation spectrum. These bands are attributed to the five 4f–5d_i (i = 1, 2, ...5) excitation bands of Ce^{3+}. The number of observed 4f–5d excitation bands is in good agreement with that of the theoretical prediction of 5d undegenerated orbitals after the crystal field splitting of Ce^{3+} in the C_1 low-symmetry [SrO_8] site of $Sr_2MgSi_2O_7$. Accordingly, the 5d crystal field splitting (CFS) energy of Ce^{3+} is evaluated to be about 2.40 eV (19.3 × 10^3 cm^{-1}) and the 5d centroid energy is about 5.08 eV (41.0 × 10^3 cm^{-1}). The 5d centroid energy of Ce^{3+} in a compound depends on the covalence between anion ligands and the 5d-orbital, and the spectroscopic polarizability of the anions in the first coordination sphere around Ce^{3+}, which are closely related to the nephelauxetic effect.[17] In the present case, the 5d centroid energy of Ce^{3+} (41.0 × 10^3 cm^{-1}) is higher than that of silicates like $Lu_2Si_2O_7$ (38.8 × 10^3 cm^{-1}) and Li_2CaSiO_4 (39.6 × 10^3 cm^{-1}).[18,19] Clearly, a relatively higher 5d centroid energy implies a weaker covalence, spectroscopic polarizability and nephelauxetic effect in this case. The 5d CFS of Ce^{3+} is significantly affected by the size and shape of the first anion coordination polyhedron around Ce^{3+}, especially the symmetry of the site, the coordination number and the Ce^{3+}–O^{2-} bond length. The 5d CFS of Ce^{3+} (2.40 eV) in the present case falls in between that of other eight-fold coordinated sites of silicates, such as the C_1 symmetry of Ba^{2+} in $BaMg_2Si_2O_7$ (1.97 eV) and the C_2 symmetry of Ca^{2+} in $CaMgSiO_6$ (2.61 eV),[5,20] which is in good agreement with the average Ce–O bond length in $Sr_2MgSi_2O_7$ (2.669 Å) between those in $BaMg_2Si_2O_7$ (2.882 Å) and $CaMgSiO_6$ (2.501 Å). With the peaks of the lowest 5d and $^2F_{5/2}$ transitions in the excitation (326 nm) and emission (345 nm) spectra, the Stokes shift was estimated to be about 0.21 eV (1.69 × 10^3 cm^{-1}), which is smaller than the average value ~0.31 eV (2.5 × 10^3 cm^{-1}) of Ce^{3+}-doped compounds and suggests a smaller electron-vibrational interaction (EVI) for the 4f–5d transitions of Ce^{3+} in $Sr_2MgSi_2O_7$.

The EVI of a Ce^{3+} impurity center is characterized by three parameters, including the Stokes shift, the Huang–Rhys factor (S) and the effective phonon energy ($\hbar\omega$). All of them describe the shift of the electronic states corresponding to the ground and excited electronic states. The value of S and $\hbar\omega$ can be estimated using eqn (1) and (2):[21]

$$\Delta E_s = (2S - 1)\hbar\omega \quad (1)$$

$$\Gamma(T) = \sqrt{8\ln 2}\hbar\omega\left[S\coth\left(\frac{\hbar\omega}{2kT}\right)\right]^{1/2} \quad (2)$$

where T is the temperature (K), $\Gamma(T)$ is the full width at half maximum (FWHM) of the emission band at temperature T, and k is the Boltzmann constant (8.62 × 10^{-5} eV K^{-1}). The $\Gamma(T)$ of the 5d to $^2F_{5/2}$ emission band at 78 K was estimated to be 1380 cm^{-1} *via* a Gaussian fit according to the experimental result shown in Fig. 2. With the solution, we can predict the

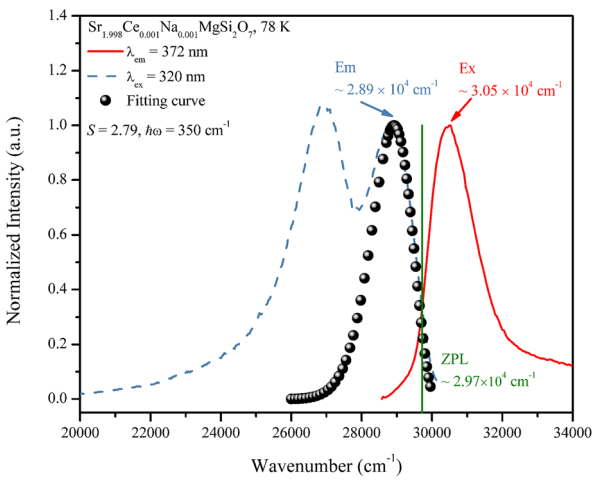

Fig. 2 The height-normalized excitation (λ_{em} = 372 nm) and emission (λ_{ex} = 320 nm) spectra of the sample $Sr_{1.998}Ce_{0.001}Na_{0.001}MgSi_2O_7$ at 78 K and the fitting curve *via* EVI analysis.

emission band of Ce^{3+} using eqn (3) and further confirm the solution validity,

$$I = \frac{e^{-S}S^p}{p!}\left(1 + S^2\frac{e^{-\frac{\hbar\omega}{kT}}}{p+1}\right), p = \frac{E_0 - E}{\hbar\omega} \quad (3)$$

where E_0 is the zero-phonon line (ZPL) energy and p is the number of effective phonons involved in the emission transition. The ZPL is located at the point of intersection of the excitation and emission spectra at 337 nm (29.7×10^3 cm^{-1}) in this case. By solving eqn (1) and (2), the acquired values are S = 2.79 and $\hbar\omega$ = 350 cm^{-1}. With these values, the best simulation of the Ce^{3+} emission band is achieved as shown in Fig. 2, which is in good agreement with the emission band shape, illustrating the validities of S and $\hbar\omega$ values. The far infrared reflectance spectrum of $Sr_2MgSi_2O_7$ is displayed in Fig. S3.† Peaks in the range of 480–1100 cm^{-1} are attributed to the stretching and bending modes of Si–O–Si, and those below 480 cm^{-1} are due to the M–O (M = Sr, Mg) stretching and bending modes.[22] Accordingly, the effective phonons should correspond to the M–O (M = Sr, Mg) stretching and bending vibrations, and the infrared spectrum verifies the validities of the fitted effective phonon energy $\hbar\omega$. Such smaller S and $\hbar\omega$ values further confirm the weak electron–phonon coupling.

Ce^{3+} doping concentration dependent luminescence is also studied as shown in Fig. S4 of the ESI.† The nearly identical spectral profiles and overlapped luminescence decay curves indicate that concentration quenching has not occurred yet in the doping range. The lifetime of Ce^{3+} at RT shown in Fig. S4(b)† is consistent with that at 78 K shown in the inset of Fig. 1, implying that temperature quenching does not occur below RT, as discussed in detail below.

Fig. 3(a) shows the excitation (λ_{em} = 372 nm) and emission (λ_{ex} = 320 nm) spectra of $Sr_{1.998}Ce_{0.001}Na_{0.001}MgSi_2O_7$ at 78–500 K. The band intensities of excitation and emission decrease significantly with the increase of the temperature. A careful examination of the excitation spectrum shows that the first excitation peak slightly moves toward the short-wavelength direction (from ~326 nm at 78 K to ~323 nm at 500 K) as the temperature increases, resulting from the decrease of Ce^{3+} 5d CFS with the lattice expansion at a higher temperature. Meanwhile, the doublet emission bands gradually merge into one broad band due to the heat-stimulated electron–phonon interaction.

The luminescence decay curves of the sample $Sr_{1.998}Ce_{0.001}Na_{0.001}MgSi_2O_7$ in Fig. 3(b) nearly overlap each other in the 78–500 K range and conform to the exponential characteristics, which manifests that thermal quenching does not occur within this temperature range, indicating the good thermal stability of Ce^{3+} luminescence. This can be further corroborated by the vacuum referred binding energy (VRBE) scheme of lanthanide ions in $Sr_2MgSi_2O_7$ as follows.

By using the experimental data including the band gap energy (7.72 eV, arrow A in Fig. 4), the centroid energy of Ce^{3+} 5d states (5.08 eV) and the lowest 5d excitation energy of Ce^{3+} (3.80 eV, arrow B) obtained above, as well as the Eu^{3+}–O^{2-} charge transfer energy (4.96 eV, arrow C) from Fig. S5,† the U value, which corresponds to the energy between Eu^{2+} and Eu^{3+} ground states, was calculated to be about 7.03 eV, and the VRBE scheme of the 4f ground states and the first 5d excited states of all trivalent and divalent lanthanide ions in $Sr_2MgSi_2O_7$ can be constructed as displayed in Fig. 4. It can be found that the energy difference (E_{dc}) between the lowest 5d multiplet ($5d_1$) of Ce^{3+} and the conduction band minimum of $Sr_2MgSi_2O_7$ is ~0.53 eV, which is larger than those in silicates such as $Sr_2Al_2SiO_7$ (0.45 eV) and $SrB_2Si_2O_8$ (0.21 eV), implying the better luminescence thermal stability of Ce^{3+} in $Sr_2MgSi_2O_7$ provided that thermal-ionization is the main cause for luminescence thermal-quenching.[23,24] In addition, the

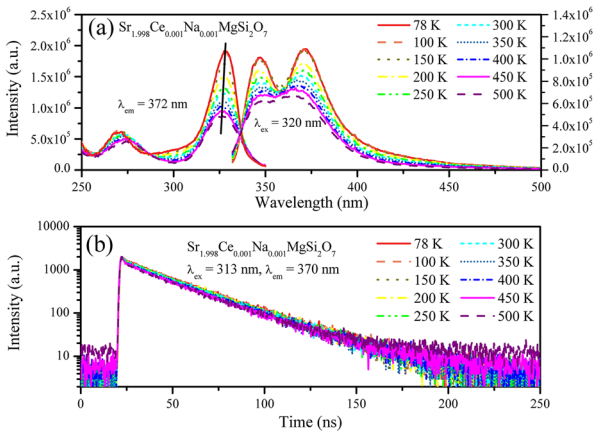

Fig. 3 (a) The excitation (λ_{em} = 372 nm) and emission (λ_{ex} = 320 nm) spectra and (b) luminescence decay curves (λ_{ex} = 313 nm, λ_{em} = 370 nm) of the $Sr_{1.998}Ce_{0.001}Na_{0.001}MgSi_2O_7$ sample in the temperature range of 78 to 500 K.

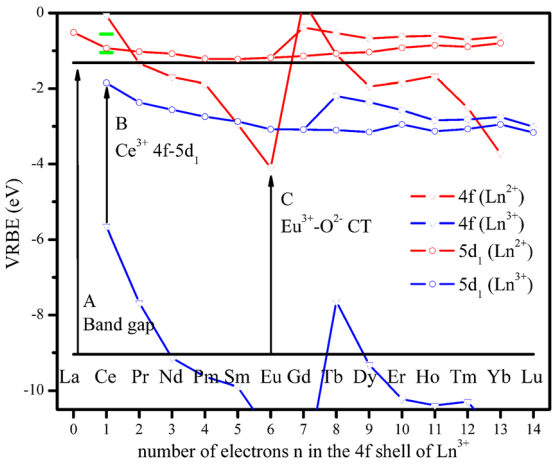

Fig. 4 The vacuum referred binding energy (VRBE) scheme of all trivalent and divalent lanthanide (Ln^{3+} and Ln^{2+}) ions in $Sr_2MgSi_2O_7$. The upper solid line is the conduction band minimum (CBM) and the lower one is the valence band maximum (VBM). The blue lines are the 4f ground states and the lowest 5d states of Ln^{3+}, while the red lines are related to Ln^{2+}. The green horizontal bars are $5d_2$ and $5d_3$ of Ce^{3+}.

short green bars in Fig. 4 depict the second and third 5d excitation states ($5d_2$, $5d_3$) of Ce^{3+} in the compound, which are located in the conduction band. This explains the weak excitation band intensities of the $4f–5d_{2,3,4,5}$ transitions in relation to the unambiguously intense $4f–5d_1$ transition shown in Fig. 1 due to the auto-ionization processes of electrons in these higher $5d_{2,3,4,5}$ excited states.[13]

3.3. Impact of the local structure on the luminescence of Ce^{3+} in $Sr_2MgSi_2O_7$, $Ba_2MgSi_2O_7$ and $BaMg_2Si_2O_7$

$Sr_2MgSi_2O_7$, $Ba_2MgSi_2O_7$ and $BaMg_2Si_2O_7$ are three typical alkaline earth pyrosilicates with similar compositions.[20,25] In these compounds, there is only one type of eight-fold coordinated Ba^{2+} or Sr^{2+} site with C_1 symmetry as listed in Table 1. The doped Ce^{3+} ions are expected to enter Ba^{2+} or Sr^{2+} sites but not occupy Mg^{2+} sites because the ionic radius of Mg^{2+} is evidently smaller than that of Ce^{3+}. Based on these structural characteristics, they should be suitable compounds to understand the dependence of luminescence properties on the local structure of Ce^{3+} in the host compounds. It is of significance to compare the structure and the band gap of the three host compounds and discuss their impact on luminescence properties such as the 5d centroid energy, the Stokes shift, the 5d CFS and the decay time of Ce^{3+} in these host compounds.

Firstly, we discuss the band gap and the band structure. From the data in Table 1, it can be found that the wavelength of the exciton peak slowly increases according to the relative order $BaMg_2Si_2O_7$ (162 nm) < $Sr_2MgSi_2O_7$ (170 nm) < $Ba_2MgSi_2O_7$ (180 nm), while the estimated band gap energy certainly follows the opposite sequence $BaMg_2Si_2O_7$ (8.12 eV) > $Sr_2MgSi_2O_7$ (7.72 eV) > $Ba_2MgSi_2O_7$ (7.27 eV). The mean band gap energy of the three compounds was calculated to be 7.70 ± 0.42 eV. The band gap is thought to be strongly dependent on the compound composition and structure. The density functional theory (DFT) study of $Ba_2MgSi_2O_7$ indicates that the valence band maximum (VBM) is dominated by O 2p states, and the conduction band minimum (CBM) is mainly formed by Ba 5d states with a small contribution from O 2p states through Ba–O bonding.[26] We speculate that the other two compounds also have similar band structures because of their similar layered structures and band gaps. The difference in the alkaline earth cations forming a single layer in the layered structure may be responsible for the slight alteration of the band gap among these three cases.[27]

Then we deal with the 5d centroid energy and the Stokes shift of Ce^{3+}. A fascinating phenomenon that the sequence of the 5d centroid energy of Ce^{3+} is consistent with the order of band gap values is found in Table 1. It shows that the wider the band gap is, the higher the 5d centroid of Ce^{3+} is. As mentioned above, the 5d centroid of Ce^{3+} is closely related to the covalence between anion ligands and the 5d-orbital of Ce^{3+}, the spectroscopic polarizability of the anions in the first coordination sphere around Ce^{3+} and/or the nephelauxetic effect. This observation seems to imply that the covalence/spectroscopic polarizability/nephelauxetic effect affects the band gap through bonding strength, but more examples need to be taken into account. Besides, the Stokes shift of the Ce^{3+} 4f–5d transition seems to increase with the decrease of the band gap of the host compound, showing that the electron-vibrational interaction is getting weaker from $Ba_2MgSi_2O_7$ to $Sr_2MgSi_2O_7$ and $BaMg_2Si_2O_7$, which further proves that the large band gap is associated with strong bonding.

Thirdly, it can be noted that the increase in the sequence of Ce^{3+} 5d CFS energy in the order of $BaMg_2Si_2O_7$ (1.97 eV) < $Ba_2MgSi_2O_7$ (2.02 eV) < $Sr_2MgSi_2O_7$ (2.40 eV) is in good agreement with the decrease in the sequence of average M–O (M = Ba or Sr) bond lengths in the order of $BaMg_2Si_2O_7$ (2.884 Å) > $Ba_2MgSi_2O_7$ (2.813 Å) > $Sr_2MgSi_2O_7$ (2.669 Å). Because the Ce^{3+} ions occupy the C_1 symmetry [MO_8] (M = Ba or Sr) sites in all three cases, the magnitude of Ce^{3+} 5d CFS is mainly decided by the site size herein. The larger the M^{2+} site size, the longer the average M–O bond length, and the smaller the Ce^{3+} 5d CFS energy.

Finally, we compare the luminescence decay time of Ce^{3+} in three cases. Fig. S6† displays a good linear relationship of λ^3 *vs.* τ for Ce^{3+} in $Sr_2MgSi_2O_7$, $Ba_2MgSi_2O_7$ and $BaMg_2Si_2O_7$, where λ (nm) is the emission peak wavelength of the $5d–^2F_{5/2}$ transition derived from Table 1 and τ (s) represents its luminescence decay time. It is widely accepted that luminescence decay is positively correlated with the emission wavelength, and the polarization effect or the local-field effect that has

Table 1 The host structure and luminescence of Ce^{3+} in $Sr_2MgSi_2O_7$, $Ba_2MgSi_2O_7$ and $BaMg_2Si_2O_7$

Host compound	$Sr_2MgSi_2O_7$	$Ba_2MgSi_2O_7$	$BaMg_2Si_2O_7$
Crystal system	Tetragonal ($P\bar{4}21m$)	Orthorhombic ($C2/c$)	Orthorhombic ($C2/c$)
Coordination number of Sr^{2+}/Ba^{2+} ions	8	8	8
Symmetry of Sr^{2+}/Ba^{2+} sites	C_1	C_1	C_1
Average bond length of Sr^{2+}/Ba^{2+}–O^{2-} (Å)	2.669	2.813	2.884
Exciton peak (nm)	170	180	162
Band gap (eV)	7.72	7.27	8.12
Ce^{3+} 5d energy (eV)	3.80, 4.61, 5.08, 5.71, 6.20	4.00, 4.25, 4.88, 5.69, 6.02	4.17, 4.48, 5.08, 5.71, 6.14
Ce^{3+} 5d centroid energy (eV)	5.08	4.97	5.12
Ce^{3+} 5d CFS (eV)	2.40	2.02	1.97
Ce^{3+} emission (eV)	3.34, 3.59	3.44, 3.69	3.73, 4.00
Ce^{3+} Stokes shift (eV)	0.21	0.31	0.17
Ce^{3+} decay time (ns)	27.2	25	19.2

been used to interpret the various lifetimes of the Ce^{3+} 4f–5d emissions in different media with the following formulas:[28]

$$\frac{1}{\tau_r} = 4.34 \times 10^{17} \times |\langle 5d|r|4f\rangle_{eff}|^2 \chi \times \frac{1}{\lambda^3} \quad (4)$$

$$\chi = n\left[\frac{(n^2+2)}{3}\right]^2 \quad (5)$$

where τ_r is the radiative lifetime (s), λ is the emission wavelength of Ce^{3+}, $\langle 5d|r|4f\rangle_{eff}$ is the effective radial integral with a best-fit value of 0.0281 nm for Ce^{3+}, χ is the enhancement factor in the virtual cavity model and n is the refractive index of the compound. Due to the good $\lambda^3 - \tau$ linear relationship, we assume that the refractive indexes of the three pyrosilicate compounds are almost the same. Accordingly, the (average) χ value is fitted to be about 4.44. The (average) refractive index of these pyrosilicates is further estimated to be 1.69, which is slightly smaller than that (1.71) of those pyrosilicates mentioned in ref. 29.

3.4. Photoluminescence of Eu^{2+} in $Sr_2MgSi_2O_7$

Fig. 5 depicts the synchrotron radiation VUV-UV excitation (λ_{em} = 470 nm, red dashed line) and emission (λ_{ex} = 355 nm, black solid line) spectra at 11 K, and the lab UV-vis excitation spectrum (λ_{em} = 470 nm, blue dash dotted line) of the sample $Sr_{1.999}Eu_{0.001}MgSi_2O_7$ at 78 K, respectively. The two spectra are in line in the 320–345 nm region. The bands in the 200–450 nm range are attributed to the 4f–5d transitions of Eu^{2+}, and those above this region are attributed to host-related absorption as mentioned in Fig. 1. The host exciton creation peak at about 172 nm is in good agreement with that observed in Fig. 1.

The sample exhibits intense cyan emission peaking at ~470 nm (2.64 eV), and its FWHM is ~1.69×10^3 cm^{-1} (0.209 eV). The energy of transition from the ground 4f multiplet to the first 5d level ($5d_1$) of Eu^{2+} is empirically estimated to be ~435 nm (2.85 eV) in terms of the wavelength at 15 to 20% of the maximum excitation intensity on the long-wavelength side.[30] Accordingly, the Stokes shift of Eu^{2+} emission was found to be ~0.21 eV, which will be used later to discuss the luminescence thermal-quenching channels. The decay curve in the inset is exponential with a decay time of ~572 ns.

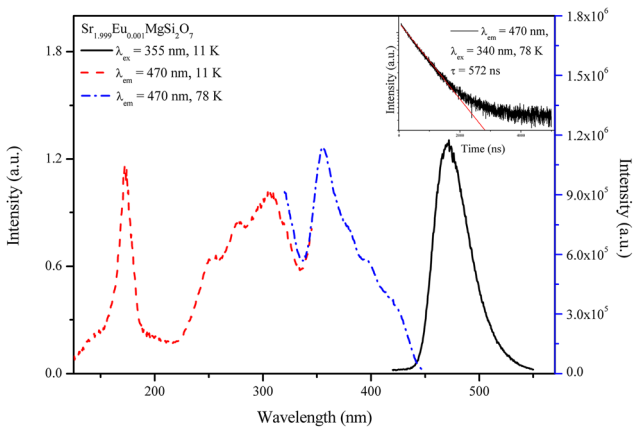

Fig. 5 The synchrotron radiation VUV-UV excitation (red dashed line, λ_{em} = 470 nm) and emission (black solid line, λ_{ex} = 355 nm) spectra at 11 K and UV-vis excitation spectra (blue dashed dot line, λ_{em} = 470 nm) at 78 K of the $Sr_{1.999}Eu_{0.001}MgSi_2O_7$ sample. The inset shows the luminescence decay curve (λ_{ex} = 340 nm, λ_{em} = 470 nm) at 78 K.

Fig. 6 shows the intensity normalized emission spectra (a, λ_{ex} = 355 nm) and luminescence decay curves (b, λ_{ex} = 340 nm, λ_{em} = 470 nm) of the sample $Sr_{1.999}Eu_{0.001}MgSi_2O_7$ at 78–450 K, respectively. The emission bands broaden steadily and the integrated intensities decrease with an increase in temperature (Fig. 6(a and c)), while the emission peaks shift by about 4 nm to the short-wavelength side. Meanwhile, the luminescence decays become rapid and start to deviate from exponential gradually (Fig. 6(b)). The evolution of decay curves implies the occurrence of thermal quenching of Eu^{2+} emission in the temperature range. The curves (c and d) display the dependencies of the integrated emission intensity and lifetime on temperature. The variations of the integrated intensity and lifetime show similar tendencies, which further confirms the earlier result.[31] According to the single-barrier-quenching model, the thermal quenching activation energy (E_a) of Eu^{2+} luminescence is estimated using eqn (6) and (7), respectively,[32]

$$I(T) = \frac{I_0}{1 + \Gamma_0/\Gamma_v \exp(-E_a/kT)} \quad (6)$$

$$\tau(T) = \frac{1/\Gamma_v}{1 + \Gamma_0/\Gamma_v \exp(-E_a/kT)} \quad (7)$$

where $I(T)$ and $\tau(T)$ are the integrated intensity and luminescence lifetime at temperature T, respectively, I_0 is the initial integrated intensity, Γ_0 is the thermal-quenching rate at $T = \infty$, Γ_v is the reciprocal of the intrinsic lifetime of Eu^{2+}, and k is the Boltzmann constant (8.62×10^{-5} eV K^{-1}). The fitting results derived from the integrated intensity and lifetime are listed in Table S1.† Γ_v values are fitted as 1.73×10^6 and 1.76×10^6 s^{-1}, respectively, corresponding to the intrinsic lifetimes of 578 ns and 568 ns, which is consistent with the data (572 ns) obtained from the decay curve at 78 K. Besides, the thermal quenching activation energy (E_a) values were evaluated to be 0.226 and 0.252 eV, respectively. So the mean E_a value was calculated to be 0.239 ± 0.013 eV.

The thermal quenching mechanism of Eu^{2+} luminescence in $Sr_2MgSi_2O_7$ can be understood with the help of this activation energy (E_a). The luminescence thermal quenching of 4f–5d transitions is thought to be the consequence of one of the following three mechanisms or their combinations:[33] (1) crossover relaxation (CR) caused by electron–phonon coupling, (2) thermally activated concentration quenching, and (3) thermal ionization of 5d electrons into the conduction band.

Firstly, the 4f–5d CR mechanism can be excluded from the present case. The energy barrier for the CR channel (E_{fd}) has been estimated to be about 2.14 eV using the first-principles study.[34] Such a large difference between the values of E_{fd} (2.14 eV) and E_a (0.239 ± 0.013 eV) strongly negates the possibility of

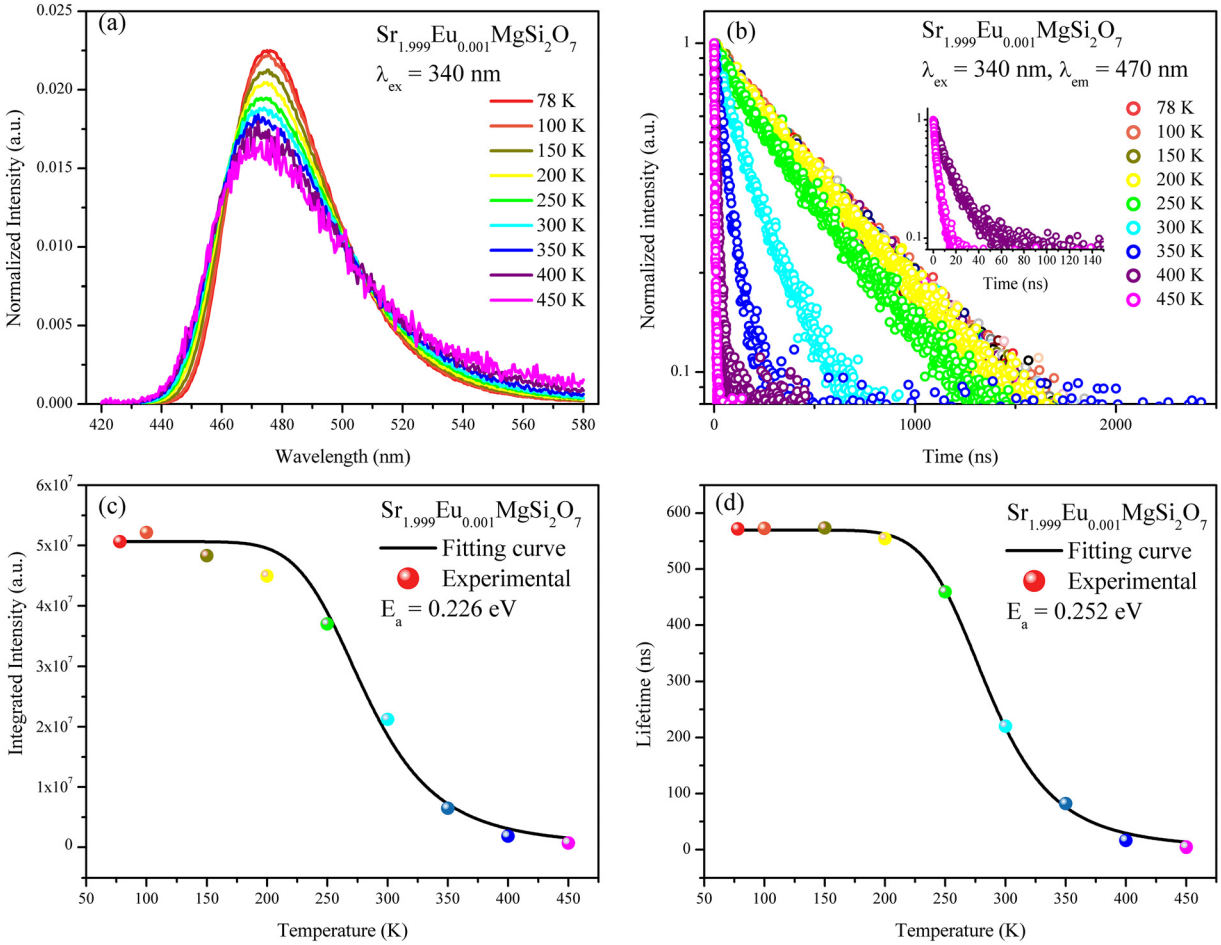

Fig. 6 (a) The intensity normalized emission spectra (λ_{ex} = 355 nm) and (b) normalized luminescence decay curves (λ_{ex} = 340 nm, λ_{em} = 470 nm) of the $Sr_{1.999}Eu_{0.001}MgSi_2O_7$ sample in the temperature range of 78–450 K. The inset in plot b shows the details of the decay curve at 400 K and 450 K. The dependencies of the integrated emission intensity (c) and lifetime (d) on temperature and the fitting curves using eqn (6) and (7).

CR as the channel for the luminescence thermal quenching of Eu^{2+} in $Sr_2MgSi_2O_7$. Besides, we assume that the thermally activated concentration quenching is also not the dominant channel for the thermal quenching of Eu^{2+} luminescence, due to the small overlap between the excitation and emission bands as shown in Fig. 5. Accordingly, the thermal ionization of 5d electrons in the conduction band should play an important role in the thermal quenching of Eu^{2+} luminescence processes. The VRBE scheme shown in Fig. 4 can illustrate the rationality of this viewpoint. The energy barrier between the lowest 5d of Eu^{2+} and the conduction band minimum (E_{dc}) is a vital parameter for thermal ionization processes. It can be found that there is only a small difference between E_{dc} (about −0.14 eV) read from the VRBE scheme in Fig. 4 and the above-mentioned E_a value (0.239 ± 0.013 eV). This smaller E_{dc} value may be related to the introduction of errors in the processes of measuring luminescence and building the VRBE scheme.[35] Besides, the measurement of luminescence and the fitting of the activation energy may also result in some errors. These factors are responsible for the discrepancies between the two estimates. Although there is a difference between the E_{dc} and E_a values, the VRBE scheme in Fig. 4 gives us a crucial indication that the lowest 5d of Eu^{2+} is close to the conduction band minimum. It is reasonable that thermal ionization is considered to be the most likely major mechanism for thermal quenching of Eu^{2+} luminescence in our case.

3.5. Energy transfer dynamics of Ce^{3+} and Eu^{2+} in $Sr_2MgSi_2O_7$

The discussions in sections 3.2 and 3.3 manifest the spectral overlap between the excitation bands of Ce^{3+} and the emission bands of Eu^{2+}, implying that Ce^{3+} ions can serve as a possible sensitizer to the luminescence of Eu^{2+} ions through energy transfer. To verify the ET from Ce^{3+} to Eu^{2+}, the luminescence properties of a series of Ce^{3+} and Eu^{2+} co-doped samples $Sr_{1.99-x}Ce_{0.005}Eu_xNa_{0.005}MgSi_2O_7$ (x = 0, 0.001, 0.005, 0.01) with a fixed Ce^{3+} concentration were measured and are shown in Fig. 7. With the increase of the Eu^{2+} concentration, the emission intensities of Ce^{3+} drop sharply and the decay curves of Ce^{3+} gradually deviate from the exponential, implying the appearance of energy transfer from Ce^{3+} to Eu^{2+}. To further study the energy transfer dynamics from Ce^{3+} to Eu^{2+}, the

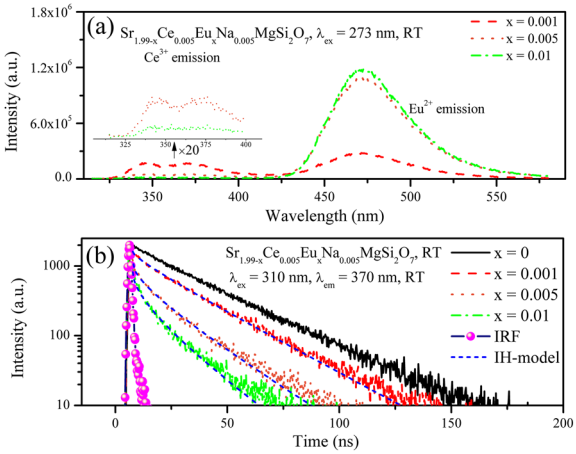

Fig. 7 (a) The emission spectra (λ_{ex} = 273 nm) of the samples $Sr_{1.99-x}Ce_{0.005}Eu_xNa_{0.005}MgSi_2O_7$ (x = 0, 0.001, 0.005, 0.01) and (b) luminescence decay curves (λ_{ex} = 310 nm, λ_{em} = 370 nm) of the samples $Sr_{1.99-x}Ce_{0.005}Eu_xNa_{0.005}MgSi_2O_7$ (x = 0.001, 0.005, 0.01) at RT and the fitting result using the Inokuti–Hirayama (IH) model (S = 6).

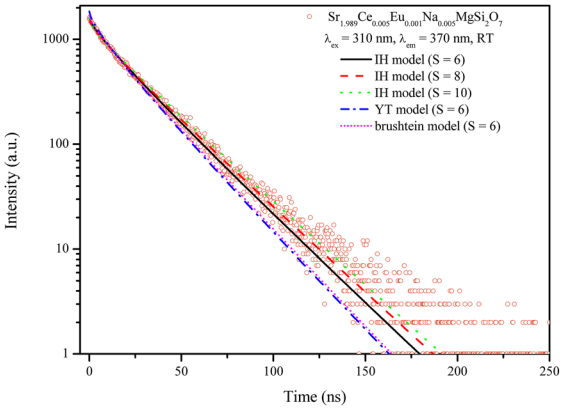

Fig. 8 The luminescence decay curve (λ_{ex} = 310 nm, λ_{em} = 370 nm) of the $Sr_{1.989}Ce_{0.005}Eu_{0.001}Na_{0.005}MgSi_2O_7$ sample at RT and the corresponding fitting curves using the Inokuti–Hirayama model (S = 6, 8, 10), Yokota–Tanimoto model (S = 6) and Burshteĭn model (S = 6).

decay curve of the sample $Sr_{1.989}Ce_{0.005}Eu_{0.001}Na_{0.005}MgSi_2O_7$ is fitted by three models as follows.

First, we only consider the energy transfer between the donor Ce^{3+} and the acceptor Eu^{2+} when energy migration between the donor Ce^{3+} ions does not exist, and the decay curve behavior can be described with the Inokuti–Hirayama (IH) model listed below,[36]

$$I(t) = I(0)\exp\left[-\left(\frac{t}{\tau_0}\right) - \frac{4\pi}{3}C_A\Gamma\left(1-\frac{3}{S}\right)(C_{DA}t)^{\frac{3}{S}}\right] \quad (8)$$

where $I(0)$ and $I(t)$ are the initial luminescence intensity and the emission intensity of Ce^{3+} at time t, respectively; τ_0 is the intrinsic luminescence lifetime of the donor Ce^{3+} (27.2 ns); C_A is the concentration of the acceptor Eu^{2+} (6.067×10^{24} m^{-3}); C_{DA} is the energy transfer microparameter; $\Gamma(1 - 3/S)$ is a gamma function; S is the multipolar effect parameter and its values are 6, 8 and 10, corresponding to the dominant mechanism being electric dipole–dipole, electric dipole–quadrupole or electric quadrupole–quadrupole interactions, respectively. To identify the main mechanism of multipolar interaction, the decay curve of the sample $Sr_{1.989}Ce_{0.005}Eu_{0.001}Na_{0.005}MgSi_2O_7$ is fitted using the Inokuti–Hirayama model with different S values, and the results are shown in Fig. 8 and Table S2.† The best fitting result (R^2 = 0.998) is obtained when S = 6, suggesting that the main mechanism of energy transfer between Ce^{3+} and Eu^{2+} is the electric dipole–dipole interaction. The C_{DA} value was estimated to be 2.89×10^{-45} m^6 s^{-1} and the critical distance R_c was found to be 20.7 Å using the relationship $\tau_0 = R_c^S/C_{DA}^{(S)}$, which implies that the energy transfer from Ce^{3+} to Eu^{2+} is effective.

In addition, the energy migration between the donor Ce^{3+} is analyzed and carefully excluded. When the distance between adjacent Ce^{3+} ions is shorter than that between the Ce^{3+} and Eu^{2+} ions, a slow energy migration may come up between Ce^{3+} and the luminescence of donor Ce^{3+} can be described using the Yokota–Tanimoto (YT) model (diffusion model),[37]

$$I(t) = I(0)\exp\left[-\left(\frac{t}{\tau_0}\right) - \frac{4\pi}{3}C_A\Gamma\left(1-\frac{3}{S}\right)(C_{DA}t)^{\frac{3}{S}} \times \left(\frac{1+10.866X+15.500X^2}{1+8.743X}\right)^{\frac{S-3}{S-2}}\right] \quad (9)$$

$$X = D \times C_{DA}^{-\frac{2}{S}} \times t^{\frac{S-2}{S}} \quad (10)$$

$$D = \frac{C_{DD}}{2(S-5)} \times \left(\frac{4\pi C_D}{3}\right)^{\frac{S-2}{S}} \quad (11)$$

where D is the diffusion parameter, C_{DD} is the energy migration parameter, C_D is the concentration of donor Ce^{3+} (3.034×10^{25} m^{-3}) and other symbols have the same meaning as above. The fitting result is also displayed in Fig. 8 and Table S2.† C_{DA} was fitted to be 2.35×10^{-46} m^6 s^{-1} while C_{DD} was 1.03×10^{-45} m^6 s^{-1}. This result does not meet the constraint of the Yokota–Tanimoto model that $C_{DD} \ll C_{DA}$, which reveals that the slow energy migration between Ce^{3+} is invalid.

Finally, the Burshteĭn model (hopping model) is applied to estimate the fast energy migration between Ce^{3+},[38]

$$I(t) = I(0)\exp\left[-\left(\frac{t}{\tau_0}\right) - \frac{4\pi}{3}C_A\Gamma\left(1-\frac{3}{S}\right)(C_{DA}t)^{\frac{3}{S}} - Wt\right] \quad (12)$$

where $W = \pi\left(\frac{2\pi}{3}\right)^{\frac{5}{2}}C_A^2(C_{DA}C_{DD})^{\frac{1}{2}}$ and other symbols are the same as those mentioned above. The fitting result is presented

in Fig. 8 and Table S2,† but C_{DA} and C_{DD} failed to satisfy the validity rule of the Burshteĭn model ($C_{DD} \gg C_{DA}$). Therefore, a conclusion can be drawn that the energy transfer between Ce^{3+} and Eu^{2+} is mainly governed by the electric dipole–dipole interaction in the sample $Sr_{1.989}Ce_{0.005}Eu_{0.001}Na_{0.005}MgSi_2O_7$ and the influence of energy migration between Ce^{3+} in a fast or slow mode is negligible. Besides, when the concentration of Eu^{2+} is further increased to x = 0.005 and 0.01 in the $Sr_{1.99-x}Ce_{0.005}Eu_xNa_{0.005}MgSi_2O_7$ samples, the luminescence decay curves of Ce^{3+} are also well described using the Inokuti–Hirayama model, as shown in Fig. 7(b).

3.6. X-ray radioluminescence of Ce^{3+} and Eu^{2+} in $Sr_2MgSi_2O_7$

Fig. 9 shows the X-ray excited luminescence spectra of the $Sr_{1.994}Ce_{0.003}Na_{0.003}MgSi_2O_7$ and $Sr_{1.997}Eu_{0.003}MgSi_2O_7$ samples at RT. To estimate the absolute light yield under X-ray excitation of these samples, a BaF_2 crystal is measured under the same experimental conditions.[13] The BaF_2 crystal presents typical self-trapped exciton emission with two bands with their maxima at ~300 and 220 nm, respectively, and its integrated intensity is specified as 8.80×10^3 ph MeV^{-1}.

The emission spectrum of the Eu^{2+} doped sample under X-ray excitation is in good agreement with that under VUV-UV excitation, and a series of extremely weak sharp peaks in the range of 550–750 nm are due to incomplete reduction of Eu^{3+} ions, but the XEL spectrum of the Ce^{3+} doped sample is somewhat different from the photoluminescence (PL) spectrum. An additional emission band above 400 nm with a peak at about 450 nm appears in the XEL spectrum but it is not observed in the PL spectrum. This additional band may be related to the emission of Ce^{3+} in impurities not detected by XRD or defects under high-energy X-ray excitation. Its integrated intensity was evaluated to be about 49.2% of the total emission by fitting the XEL spectrum of Ce^{3+} with a sum of three Gaussian functions [Ce^{3+} 5d–^2F_J (J = 5/2, 7/2) bands and the additional 450 nm emission]. According to the measured light output value of 2.81×10^3 ph MeV^{-1}, the light yield of the $Sr_{1.994}Ce_{0.003}Na_{0.003}MgSi_2O_7$ sample was estimated to be 1.47×10^3 ph MeV^{-1} after subtracting the 450 nm emission, and that of the $Sr_{1.997}Eu_{0.003}MgSi_2O_7$ sample was found to be about 5.97×10^3 ph MeV^{-1}. The low light output implies that these materials are not suitable X-ray detecting phosphors.

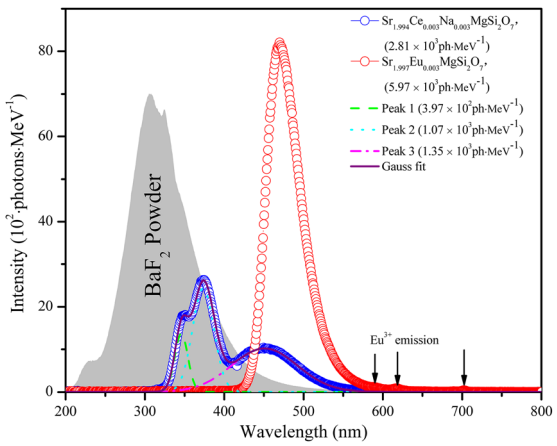

Fig. 9 The XEL spectra of the samples $Sr_{1.994}Ce_{0.003}Na_{0.003}MgSi_2O_7$, $Sr_{1.997}Eu_{0.003}MgSi_2O_7$ and crystal BaF_2 at RT, and the Gaussian fitting of the XEL spectrum of $Sr_{1.994}Ce_{0.003}Na_{0.003}MgSi_2O_7$.

4. Conclusions

This paper studies the 4f–5d transitions and the energy transfer of Ce^{3+} and Eu^{2+} in $Sr_2MgSi_2O_7$ after the preparation of the samples by a traditional high-temperature solid-state reaction method. (1) The synchrotron radiation VUV-UV excitation spectrum of the sample $Sr_{1.998}Ce_{0.001}Na_{0.001}MgSi_2O_7$ at 10 K reveals that the five 4f–5d$_i$ (i = 1, 2, ..., 5) transitions of Ce^{3+} in the C_1 low-symmetry [SrO_8] site of $Sr_2MgSi_2O_7$ are located at about 326, 269, 244, 217 and 200 nm, respectively, and the band intensities can be explained using the vacuum referred binding energy (VRBE) scheme. Typical doublet emission bands of Ce^{3+} are found with their maxima at about 345 and 368 nm, and the luminescence decay time is about 27.2 ns. The electron-vibrational interaction (EVI) analysis shows that the Huang–Rhys factor (S) and the effective phonon energy ($\hbar\omega$) are S = 2.79 and $\hbar\omega$ = 350 cm^{-1} for the 4f–5d transitions of Ce^{3+} in $Sr_2MgSi_2O_7$, respectively. The measurements on the luminescence decay behaviours show that concentration quenching does not occur in $Sr_{2-2x}Ce_xNa_xMgSi_2O_7$ samples for x values within 0.03, and the $Sr_{1.998}Ce_{0.001}Na_{0.001}MgSi_2O_7$ sample does not undergo thermal quenching below 500 K. Comparison of the luminescence properties of Ce^{3+} in a series of host compounds $Sr_2MgSi_2O_7$, $Ba_2MgSi_2O_7$ and $BaMg_2Si_2O_7$ with similar compositions indicates that the crystal field splitting (CFS) of Ce^{3+} 5d increases with the decrease of the site size, while the 5d centroid energy of Ce^{3+} and the Stokes shift are closely associated with the band gap. The third power of the emission wavelength of Ce^{3+} in three compounds shows a good linear relationship with the luminescence decay time, which may be related to similar refractive indexes of these pyro-silicates. (2) The 4f–5d excitation bands of Eu^{2+} covers the 200–450 nm range, the cyan emission peaks at about 470 nm (2.64 eV) with a FWHM of around 1687 cm^{-1} and the decay time is approximately 572 ns. The thermal quenching activation energy of Eu^{2+} luminescence was estimated to be about 0.239 ± 0.013 eV by the dependencies of the lifetime and intensity on temperature. Accordingly, the thermal ionization mechanism is thought to be the main thermal quenching channel. (3) Systematic studies of the luminescence decay curves with three luminescence dynamic models suggest that the energy transfer from Ce^{3+} to Eu^{2+} is mainly through electric dipole–dipole interactions and the energy migration between Ce^{3+} in a fast or slow mode is negligible. (4) The low light outputs of the Ce^{3+} and Eu^{2+} doped materials under X-ray exci-

tation suggest that phosphors are not suitable for X-ray detection.

Conflicts of interest

There are no conflicts to declare.

Acknowledgements

This work was financially supported by the National Natural Science Foundation of China (Grant No. 22171290, 52161135110) and the Natural Science Foundation of Guangdong Province (2022A1515011376). The vacuum ultraviolet (VUV) and far-infrared (IR) reflection spectral measurements of the samples were carried out with the support of the 4B8 beamline at the Beijing Synchrotron Radiation Facility (BSRF, Beijing, China) and the BL01B beamline at the National Synchrotron Radiation Laboratory (NSRL, Hefei, China), respectively.

References

1 P. Dorenbos, Fundamental limitations in the performance of Ce^{3+}-, Pr^{3+}-, and Eu^{2+}- activated scintillators, *IEEE Trans. Nucl. Sci.*, 2010, **57**, 1162–1167.
2 C. R. Ronda, *Luminescence: from theory to applications*, Wiley, Weinheim, 2007.
3 W. Lü, J. S. Huo, Y. Feng, S. Zhao and H. P. You, Photoluminescence, energy transfer and tunable color of Ce^{3+}, Tb^{3+} and Eu^{2+} activated oxynitride phosphors with high brightness, *Dalton Trans.*, 2016, **45**, 9676–9683.
4 C. Li, H. W. Zheng, H. W. Wei, S. J. Qiu, L. Xu, X. M. Wang and H. Jiao, A color tunable and white light emitting $Ca_2Si_5N_8$:Ce^{3+}, Eu^{2+} phosphor via efficient energy transfer for near-UV white LEDs, *Dalton Trans.*, 2018, **47**, 6860–6867.
5 F. Su, B. B. Lou, Y. Y. Ou, Y. L. Yang, W. J. Zhou, C. K. Duan and H. B. Liang, VUV–UV–vis luminescence, energy transfer dynamics, and potential applications of Ce^{3+}- and Eu^{2+}-doped $CaMgSi_2O_6$, *J. Phys. Chem. C*, 2021, **125**, 5957–5967.
6 J. Y. Ding, Q. X. Xu, J. Z. He, W. B. Zhang, J. C. Zhou and Q. S. Wu, Full spectrum light-emitting diodes based on a new efficient zirconium silicate green phosphor for healthy lighting, *Mater. Chem. Front.*, 2021, **5**, 7251–7258.
7 M. Kimata, The structural properties of synthetic Sr-åkermanite, $Sr_2MgSi_2O_7$, *Z. Kristallogr. – Cryst. Mater.*, 1983, **163**, 295–304.
8 Z. G. Xiao and Z. Q. Xiao, Long persistence luminescent silicate material and its producing method, *CHN Pat*, 98105078.6, 1998.
9 Y. Q. Li and Y. H. Wang, Enhancement of long-persistence by Ce^{3+} co-doping in $Sr_2MgSi_2O_7$:Eu^{2+}, Dy^{3+} blue phosphor, *J. Phys.: Conf. Ser.*, 2009, **152**, 012090.
10 H. Homayoni, S. Sahi, L. Ma, J. Y. Zhang, J. Mohapatra, P. Liu, A. P. Sotelo, R. T. Macaluso, T. Davis and W. Chen, X-ray excited luminescence and persistent luminescence of $Sr_2MgSi_2O_7$:Eu^{2+}, Dy^{3+} and their associations with synthesis conditions, *J. Lumin.*, 2018, **198**, 132–137.
11 A. A. Coelho, *TOPAS-Academic (version 4.1), Coelho Software*, Brisbane, Australia, 2007.
12 F. Su, W. J. Zhou, Y. L. Yang, Y. Y. Ou, Z. M. Qi, C. K. Duan, M. G. Brik, P. Dorenbos and H. B. Liang, Structure, luminescence of Eu^{2+} and Eu^{3+} in $CaMgSi_2O_6$ and their co-existence for the excitation-wavelength/temperature driven colour evolution, *Dalton Trans.*, 2021, **50**, 10050–10058.
13 Y. L. Yang, B. B. Lou, Y. Y. Ou, F. Su, C. G. Ma, C. K. Duan, P. Dorenbos and H. B. Liang, Experimental and theoretical studies of site occupancy and luminescence of Ce^{3+} in $LiSr_4(BO_3)_3$ for potential X-ray detecting applications, *Inorg. Chem.*, 2022, **61**, 7654–7662.
14 A. A. Setlur and A. M. Srivastava, On the relationship between emission color and Ce^{3+} concentration in garnet phosphors, *Opt. Mater.*, 2007, **29**, 1647–1652.
15 L. Y. Zhou, F. W. Liu, R. G. Ye, L. Lei, W. G. Guo, L. Chen, D. G. Deng and S. Q. Xu, Tunable photoluminescence and temperature sensing properties of Ce^{3+}, Eu^{2+} co-doped $Ca_{2-x}Sr_xMgSi_2O_7$ phosphors, *J. Lumin.*, 2021, **240**, 118417.
16 P. Dorenbos, Charge transfer bands in optical materials and related defect level location, *Opt. Mater.*, 2017, **69**, 8–22.
17 P. Dorenbos, The nephelauxetic effect on the electron binding energy in the $4f^q$ ground state of lanthanides in compounds, *J. Lumin.*, 2019, **214**, 116536.
18 L. Pidol, B. Viana, A. K. Harari, A. Galtayries, A. Bessière and P. Dorenbos, Optical properties and energy levels of Ce^{3+} in lutetium pyrosilicate scintillator crystal, *J. Appl. Phys.*, 2004, **95**, 7731–7737.
19 P. Dorenbos, L. Pierron, L. Dinca, C. W. E. van Eijk, A. Kahn-Harari and B. Viana, 4f–5d spectroscopy of Ce^{3+} in $CaBPO_5$, $LiCaPO_4$ and Li_2CaSiO_4, *J. Phys.: Condens. Matter*, 2003, **15**, 511–520.
20 Y. Y. Ou, W. J. Zhou, C. M. Liu, L. T. Lin, M. G. Brik, P. Dorenbos, Y. Tao and H. B. Liang, Vacuum referred binding energy scheme, electron–vibrational interaction, and energy transfer dynamics in $BaMg_2Si_2O_7$:Ln (Ce^{3+},Eu^{2+}) phosphors, *J. Phys. Chem. C*, 2018, **122**, 2959–2967.
21 M. Nazarov, B. Tsukerblat and D. Y. Noh, Vibronic coupling parameters and Stokes shift in thiogallate phosphors, *J. Phys. Chem. Solids*, 2008, **69**, 2605–2612.
22 P. Makreski, G. Jovanovski, B. Kaitner, A. Gajović and T. Biljan, Minerals from Macedonia XVIII. Vibrational spectra of some sorosilicates, *Vib. Spectrosc.*, 2007, **44**, 162–170.
23 L. T. Lin, R. Shi, R. F. Zhou, Q. Peng, C. M. Liu, Y. Tao, Y. Huang, P. Dorenbos and H. B. Liang, The effect of Sr^{2+} on luminescence of Ce^{3+}-doped $(Ca,Sr)_2Al_2SiO_7$, *Inorg. Chem.*, 2017, **56**, 12476–12484.
24 Q. Peng, C. M. Liu, D. J. Hou, W. J. Zhou, C. G. Ma, G. K. Liu, M. G. Brik, Y. Tao and H. B. Liang, Luminescence of Ce^{3+}-doped $MB_2Si_2O_8$ (M = Sr, Ba): a

deeper insight into the effects of electronic structure and Stokes shift, *J. Phys. Chem. C*, 2016, **120**, 569–580.

25 J. Yan, C. M. Liu, J. Vlieland, J. B. Zhou, P. Dorenbos, Y. Huang, Y. Tao and H. B. Liang, Intense emission of $Ba_2MgSi_2O_7$:Eu^{2+} under X-ray excitation for potential detecting applications, *J. Lumin.*, 2017, **183**, 97–101.

26 J. Yan, L. X. Ning, Y. C. Huang, C. M. Liu, D. J. Hou, B. B. Zhang, Y. Huang, Y. Tao and H. B. Liang, Luminescence and electronic properties of $Ba_2MgSi_2O_7$:Eu^{2+}: a combined experimental and hybrid density functional theory study, *J. Mater. Chem. C*, 2014, **2**, 8328–8332.

27 J. Hölsäa, T. Laamanena, M. Lastusaaria and P. Novák, Isolated defects in $Sr_2MgSi_2O_7$: a DFT study, *Phys. Procedia*, 2012, **29**, 76–85.

28 C. K. Duan and M. F. Reid, Local field effects on the radiative lifetimes of Ce^{3+} in different hosts, *Curr. Appl. Phys.*, 2006, **6**, 348–350.

29 I. Petousis, D. Mrdjenovich, E. Ballouz, M. Liu, D. Winston, W. Chen, T. Graf, T. D. Schladt, K. A. Persson and F. B. Prinz, Data descriptor: High-throughput screening of inorganic compounds for the discovery of novel dielectric and optical materials, *Sci. Data*, 2017, **4**, 160134.

30 P. Dorenbos, Relation between Eu^{2+} and Ce^{3+} f ↔ d-transition energies in inorganic compounds, *J. Phys.: Condens. Matter*, 2003, **15**, 4797–4807.

31 A. A. Setlur, A. M. Srivastava, L. Pham, M. Hannah and U. Happek, Charge creation, trapping, and long phosphorescence in $Sr_2MgSi_2O_7$:Eu^{2+}, RE^{3+}, *J. Appl. Phys.*, 2008, **103**, 053513.

32 M. D. Birowosuto, P. Dorenbos, C. W. E. van Eijk, K. W. Kramer and H. U. Güdel, Thermal quenching of Ce^{3+} emission in PrX_3 (X = Cl, Br) by intervalence charge transfer, *J. Phys.: Condens. Matter*, 2007, **19**, 256209.

33 Y. C. Lin, M. Bettinelli and M. Karlsson, Unraveling the mechanisms of thermal quenching of luminescence in Ce^{3+}-doped garnet phosphors, *Chem. Mater.*, 2019, **31**, 3851–3862.

34 Y. C. Jia, A. Miglio, S. Poncé, M. Mikami and X. Gonze, First-principles study of the luminescence of Eu^{2+}-doped phosphors, *Phys. Rev. B*, 2017, **96**, 125132.

35 P. Dorenbos, Mechanism of persistent luminescence in $Sr_2MgSi_2O_7$:Eu^{2+}; Dy^{3+}, *Phys. Status Solidi B*, 2005, **242**, R7–R9.

36 M. Inokuti and F. Hirayama, Influence of energy transfer by the exchange mechanism on donor luminescence, *J. Chem. Phys.*, 1965, **43**, 1978–1989.

37 I. R. Martin, V. D. Rodríguez, U. R. Rodríguez-Mendoza and V. Lavin, Energy transfer with migration. Generalization of the Yokota–Tanimoto model for any kind of multipole interaction, *J. Chem. Phys.*, 1999, **111**, 1191–1194.

38 A. I. Burshteĭn, The influence of the migration mechanism of approaching particles on the energy transfer between them, *J. Lumin.*, 1980, **21**, 317–321.